Ultrasonic-Based Stress Identification of a Reinforced Concrete Beam via USR-Net

Zheng Gang[1,2(✉)], Yu Jigang[1], Gu Zhuangzhuang[3], and Zhang Benniu[1,2]

[1] Chongqing Jiaotong University, Nanan District, Chongqing, China
zhenggang@cqjtu.edu.c
[2] State Key Laboratory of Mountain Bridge and Tunnel Engineering, Chongqing, China
[3] University of South Carolina, Columbia, USA

Abstract. In recent two decades, though great progress has been made in stress identification of reinforced concrete structures using the ultrasonic-based coda wave interference technics, the state of art techniques in this field seems to be capable of considering only a single loading pattern. To address this issue, in this paper, a USR-Net based on DL algorithm is proposed for stress identification of reinforced concrete beams under two different load patterns. It is featured by a successive use of S-transform and Residual Blocks, with the latter's conventional "square" convolution kernel replaced by a "flat" one, which gives play to the pictorial characteristics of the time-frequency matrix from the former for a more efficient and accurate stress recognition. The effectiveness of USR-Net is validated on experimental tests of two concrete I-beams under respectively a three-point bending and an eccentric compression load. Compared with traditional non-DL ultrasonic based algorithms, the USR-Net is more adaptive for different load patterns and robust to noises, providing a potentially novel solution for stress identification of practical concrete structures.

Keywords: Ultrasonic coda wave · Concrete stress · Deep learning · Residual block

1 Introduction

The most frequently employed approach for evaluating stress in reinforced concrete structures involves measuring changes in strain within structural members. But, the installation and removal of strain gauges can be a time-consuming process, especially for larger structures such as bridges. In addition, strain gauges can only measure stress changes caused by loading/unloading, or by thermal expansion and contraction-induced creep. They cannot measure the actual stress of structural components, such as permanent load stress [1]. Core drilling and slot cutting are currently widely used techniques for measuring the total stress of concrete structures. However, these techniques rely on the assumption that concrete is linearly elastic, and that stress distribution along depth is uniformly, which does not correspond to the actual situation [2]. Moreover, these methods damage concrete members and are limited in their ability to provide accurate and reliable measurements.

D. Pavlou et al. (Eds.): OES 2023, SI 29, pp. 58–79, 2024.
https://doi.org/10.1007/978-3-031-49791-9_5

In recent two decades, with the development of ultrasonic non-destructive (NDT) techniques, researchers have begun investigating the use of linear and nonlinear acoustic waves for direct stress measurement in concrete members, like coda wave measurement. Coda waves are secondary waves [3] that are generated by the scattering of primary waves within a medium. One of the primary advantages of using coda waves is their high sensitivity to small changes in mediums, allowing for precise measurements [4]. Also, coda wave measurement has the advantage of real-time monitoring of stress changes over time [5]. This is useful for identifying changes in stress caused by environmental loads or changes in permanent loads.

Previous works have devoted lots of efforts on applying coda wave to measure stress, Taylor series expansion and coda wave interferometry were utilized for coda wave measurement. Snieder [6] first proposed the concept of coda wave interference, demonstrating its sensitivity to medium changes and utilizing it to quantitatively measure changes in coda wave velocity. Payan [7, 8] used coda wave interference to study the functional relationship between the relative change rate of concrete wave velocity and stress, and extracted the third-order nonlinear coefficient of concrete materials. Ali Hafiz [9] used Coda Wave Comparison (CWC) technique to measure changes in the internal stress that are not observable on the surface of concrete. Clau [10] links essential key parameters computed from the coda wave signals to concrete structural state variables.

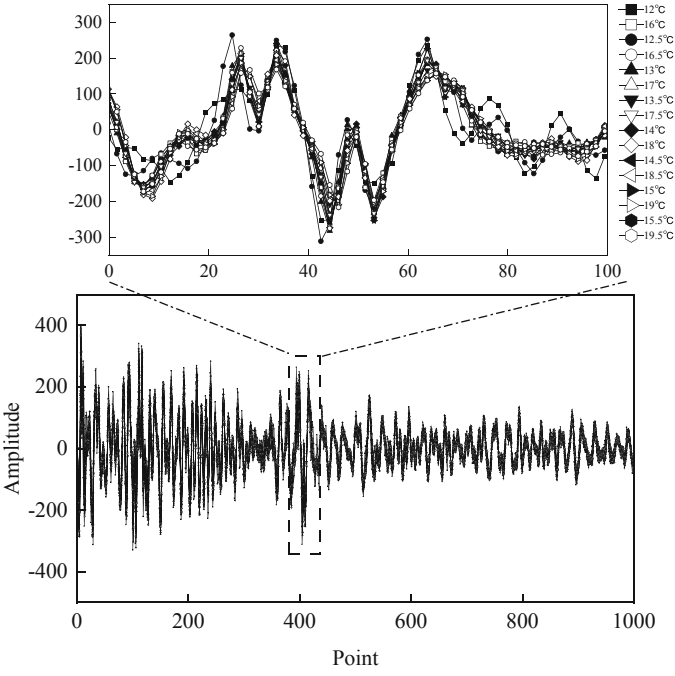

Fig. 1. Coda wave signal under same stress from different temperature.

However, these algorithms have 4 main limitations as below. (1) The amplitude of coda wave signals is typically small, making them susceptible to random noise (such as electronic noise, environmental noise, sensor noise, harmonic distortion, attenuation and reflation, etc.) and decreasing the signal quality, ultimately affecting the accuracy of stress measurement [11]. (2) Measurement results from traditional algorithms are influenced by the measurement environment, such as temperature (see Fig. 1), humidity, and noise [12, 13]. (3) These techniques require preprocessing of input data to extract relevant features, such as frequency, pulse-wave velocity, amplitude and spectrum area [1, 14, 15], that is related to the performance of the instrument and test environment. The stress recognition method of a specific parameter has poor resistance to interference, and the misjudgment rate will increase once the raw signal is polluted by noise.

To address these problems, based on the signal analysis of S-transform, innovating and improving the coda wave measurement stress method by introducing the residual Block, this study proposes USR-Net (ultrasonic-based S-transform with Residual Block Net), a deep learning model for ultrasonic-based concrete stress identification, outperforms the state-of-the-art method on identification accuracy. By extracting the time-domain and frequency-domain features of the coda wave signal comprehensively, it can effectively provide accurate stress prediction results under various loading patterns in a constantly changing environment. USR-Net provides an effective, accurate, and adaptive stress measurement method for construction monitoring, health detection, etc.

Comparing with traditional coda wave measurement methods (non-DL methods) that depend on the single time domain signal or frequency domain signal, the S-transform in the top of USR-Net can convert the raw coda wave signal into the time-frequency domain [16, 17]. By adding filters and threshold processing after S-transform to remove time-frequency components below a certain amplitude threshold, it removes random noise and improves signal quality [18, 19]. In addition, the time-frequency spectrogram output by S-transform can be analyzed and interpreted to extract frequency features [20, 21], instantaneous frequency, amplitude information, which eliminates the limitation of traditional coda wave measurement algorithms that are limited to specific signal parameters and solves the problem of weak anti-interference ability of non-DL methods. To solve the problem of interference from environmental changes on the stability of coda wave signals, the USR-Net uses multi-layer Residual Blocks to enhance feature extraction capabilities and improve the key feature extraction capabilities of coda wave signals under various environments [22]. Furthermore, the introduction of Residual Blocks improves the classification accuracy and robustness of the USR-Net [23]. Therefore, the USR-Net improves the resistance of coda wave measurement to random noise and environmental interference, as well as the ability to extract key features. This method can quickly and accurately predict the stress of concrete structures, and the real-time characteristics of USR-Net have application prospects in real-time monitoring. This study highlights the potential of deep learning algorithms in monitoring the health of concrete structures and contributes to the development of more precise and effective stress measurement techniques.

2 USR-Net

2.1 Overview

USR-Net aims to identify accurate concrete stress from the coda wave signals collected under various stress of two load patterns by solving these challenges. This could enable many new applications in stress measurement, cracks detection in practical engineering under challenging environment, like continuous changing temperature and humidity. As Fig. 2 shows, USR-Net consists of two modules: (1) S-transform-based Time-frequency Analyzer and Filter (STA and STF), which analyzes and visualizes signals in both time and frequency domains, enabling more accurate representation of the time-frequency characteristics. It can filter and denoise the raw signal to improve signal quality and reliability. (2) Feature Extractor with Residual Blocks and Classifier, which enable adaptively learn features from the visual output of STA and accurately predict stress. In the USR-Net as Fig. 2, we firstly input coda wave signal into STF to filter and denoise, and then utilize STA to analyze the denoised signal and obtain the time-frequency spectrogram image (TF-image). Finally, the Feature Extractor will extract the features from the TF-image and the Classifier classify these features and output the predicted result.

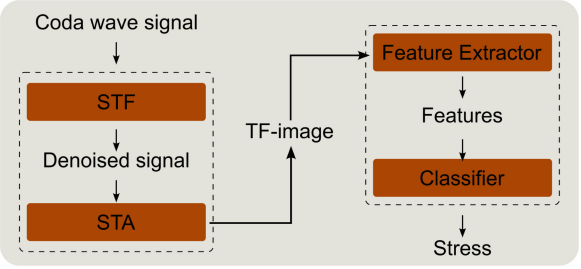

Fig. 2. USR-Net overview.

2.2 STF and STA

The core objective of this module is to denoise the raw coda wave signal and transform the denoised signal to the TF-image. The STF utilizes the multiscale and multidirectional decomposition property of the S-transform to decompose the signal into sub-signals with different scales and directions. The signal is then denoised by adjusting the threshold of the sub-signals. The STA utilizes the superior properties of the S-transform in both the time and frequency domains to transform denoised signal into the time-frequency domain for analysis.

Basic Theory of STF STF is a method based on S-transform used for filtering signal, we refer to some practices of previous works [16, 24, 25], such as threshold filtering method to filter the decomposed signal and inverse S-transform to reconstruct the filtered signal. In the process of signal processing, we find that these methods have a good effect on the removal of random Gaussian noise. The implementation of STF mainly involves the following steps:

Nomenclature

f	frequency	Hz
j	imaginary part	
N	signal length	
t	time	s
$h(t)$	signal on time	
$h'(t)$	denoised signal	
X	signal on frequency	
τ	time location	s
S	S-transform result	
S'	nverse S-transform result	

Step 1: Compute the S-transform.

Input a coda wave signal, compute its S-transform amplitude spectrum at different scales and orientations according to specified parameters. The S-transform is a time-frequency analysis technique proposed by Stockwell et.al [24, 26] and defined as Eq. 1.

$$S(\tau, f) = \int_{-\infty}^{+\infty} h(t) \underbrace{\frac{|f|}{\sqrt{2\pi}} e^{-(\tau - t)^2 f^2/2}}_{\text{Window}} e^{-j2\pi ft} dt \tag{1}$$

Step 2: Thresholding.

Thresholding on the S-transform amplitude spectrum, setting values below a certain threshold to zero, thus reducing the impact of noise. The function of thresholding as Eq. 2.

$$S'(\tau, f) = \begin{cases} S(\tau, f), \ |S(\tau, f)| > threshold \\ 0 \, otherwise \end{cases} \tag{2}$$

The threshold is determined by the following formula (48):

$$thereshold = \sqrt{2 \log_2(N)}$$

Step 3: Inverse S-transform.

An inverse S-transform on the thresholded S-transform amplitude spectrum to obtain the filtered signal. The formula for inverse S-transform is Eq. 3.

$$h'(t) = \int_{-\infty}^{\infty} \left\{ \int_{-\infty}^{\infty} S'(\tau, f) d\tau \right\} e^{j2\pi ft} df \tag{3}$$

Basic Theory of STA STA module includes two parts: DOST (Discrete Orthogonal S-transform) and Rearrange-DOST (Rearranged Discrete Orthogonal S-Transform). The DOST [26–28] is a type of Discrete Orthogonal S-transform used for decomposing signals in the time-frequency domain and extracting local features of the signal.

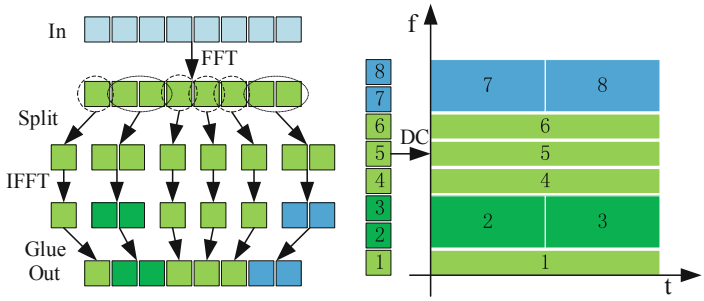

Fig. 3. The processing of DOST (left) and rearrange-DOST (right).

Rearrange-DOST is an operation that rearranges the results of the S-transform to reduce the interference of noise signals. Algorithm 1 shows the processing steps [29].

Algorithm 1 S-transform-based Time-frequency Analyzer

1: **Input:** denoised coda wave signals by STF W, sampling number n, signal length N, sampling interval t.
2: **Output:** Time-frequency spectrogram image Datasets TD.
3: **Initialize:** a 4D array TD.
4: **for** each signal x **in** W **do**
5: Process x by normalized and centered FFT, save it to x',
$$X_k = \frac{1}{\sqrt{N}} \sum_{n=0}^{N-1} x_n e^{-i2\pi kn/N}, k = 0,1,\cdots,N-1.$$
6: Calculate the bandwidth partitioning for the dost $dostbw$,
$$dostbw = \frac{2\pi}{N \Delta_t \min\left(|\Delta S|\right)}.$$
7: Split the x' according to $dostbw$ and process by normalized and centered IFFT according to $dostbw$.
Calculate $X_k = x'\left(dostbw\right), x_n = \frac{1}{\sqrt{N}} \sum_{k=0}^{N-1} X_k e^{i2\pi kn/N}, n = 0,1,\cdots,N-1.$
Save the result to the DOST coefficient $DOST$.
8: Rearrange the DOST coefficients $DOST$ in a matrix form $rearrangeDOST$, $rearrangeDOST = DOST\left(dostbw, N./dostbw\right)$.
9: Show the time-frequency spectrogram image according to $rearrangeDOST$ and save the RGB matrix to TD.
10: **end for.**
11: **return** TD.

As Fig. 3 shows [30], firstly, input the denoised signal and process it by normalized and centered FFT. Normalization is to make the transformation between the forward FFT and inverse FFT symmetric, while also ensuring the equivalence of unit energy in the time and frequency domains. Centering refers to making the result of FFT symmetric from the zero point in the frequency domain, making it more convenient for representing

real numbers. Secondly, calculate the bandwidth partitioning parameters (*dostbw*) for the DOST [26], for DOST analysis, a dyadic partitioning strategy is commonly used to divide the S-plane into a series of frequency bands with equal bandwidth, where each band's bandwidth is equal to the *dostbw*. This allows for selecting a series of rectangular regions on the S-plane and performing DOST analysis on the signal within each region to obtain time-frequency domain information. Specifically, the S-plane is divided into a group of square regions centered at the origin, with boundaries formed by dyadic partitioning from negative infinity to positive infinity, i.e., $[-2^k, 2^k] \times [-2^k, 2^k]$, where k is an integer. The signal within each region is analyzed with DOST to obtain the corresponding time-frequency domain information. Split the frequency-domain signal obtained through normalized and centered FFT to some segments according to *dostbw*, and use normalized and centered IFFT processing for each segment of the frequency-domain signal to obtain the DOST coefficients (DC). Thirdly, rearrange the DOST coefficient according to the frequency or time sequence as a pixel value of a time-frequency spectrum graph that can be represented in different colors [31]. After time-frequency domain spectral graph pixel value of all time is calculated, by composing all the pixel values into a matrix, the time-frequency domain spectral graph is obtained. It can be graphically displayed in order to visually observe the change of the signal in the time-frequency domain [27].

In general, DOST can provide more comprehensive time-frequency domain information, while rearrange DOST processing can transform it into a more easily understandable frequency-time distribution via TF-image. The TF-image can display transient and periodic information of the signal, which is an essential tool commonly used in signal processing and analysis. We analyze the coda wave signals from Stress = 1 to 10 under the same environment via STA and STF, the TF-images are shown in Fig. 4.

2.3 Feature Extractor with Residual Blocks and Classifier

From Fig. 4, the TF-images under various stresses perform significant difference, which can be seen as the key features that represent corresponding stress. We assume that the test environment is same due to the test interval of short period is short. Thus, these differences are caused only by stress changes. It is difficult to quantify this difference in time domain and frequency domain at the same time for previous works, since they acquire the features only from time domain signal or frequency domain signal. To address the limitation, we design the Feature Extractor with Residual Blocks (RB) and Classifier, which aim to extract key features from the time-frequency spectrogram and identify stress. Specially, the Feature Extractor with Residual Blocks is stacked by a set of RBs. The shortcut connection of RB [32, 33] adds the input of the Residual Block to its output, which allows the network to learn the residual mapping between the two, that makes contribution to keep detailed local features and extract fine global features [34]. The Classifier is responsible for classifying the features produced from the Feature Extractor and predicting the probability of corresponding label.

In this study, Feature Extractor with Residual Blocks includes the first convolution layer, four RBs and global average layer (GAP) as Fig. 5 shows [35]. The TF-images (size: 224*224*3, RGB image) will be input into the first convolution layer for feature extraction and the number of channels will be briefly expanded from 3 to 64. Then the features will be passed into four RBs. With layers deeper, the size of feature map is

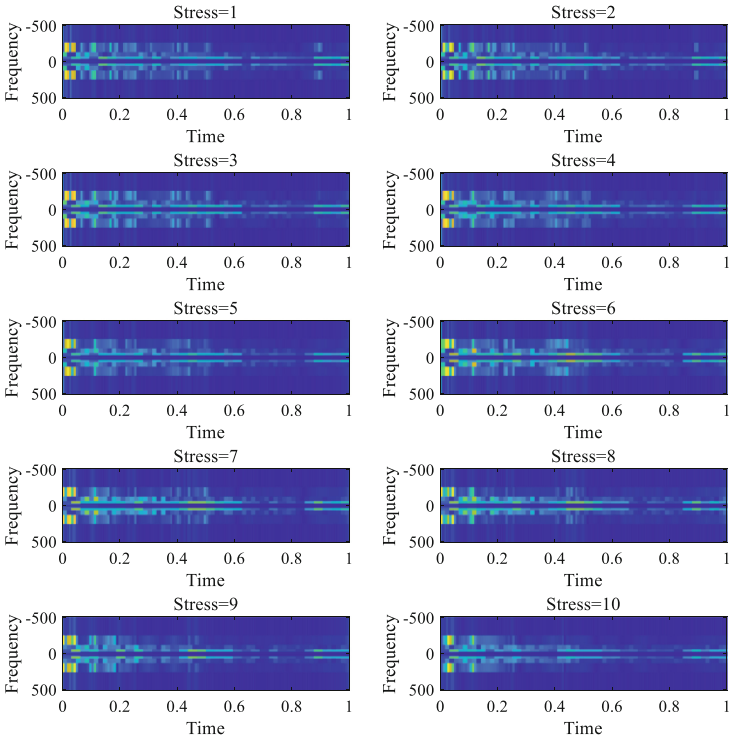

Fig. 4. The TF-images of three-point bending experiment under the same environment (the image size is 224*224*3).

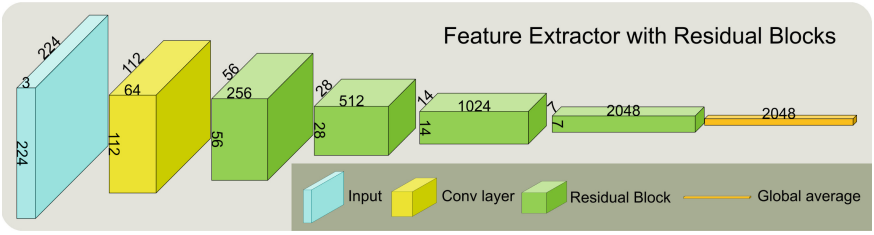

Fig. 5. The architecture of Feature Extractor.

reduced, and the channel number will be expanded. The parameters of Feature extractor and Classifier are shown in Table 1 [36, 39]. Reducing the size of feature map while extracting global features can accelerate the training process. Also, the reduced feature maps enable convolution filters to see a bigger region, which allows model to capture global features of TF-images [37]. Finally, we use 2 linear layers for classifying the extracted features into 20 stress levels.

Table 1. The parameter of Feature Extractor with residual blocks and classifier.

Layer name	Parameter	Output size
Conv	$7 \times 7, 64$, stride 2	$112 \times 112 \times 64$
Residual Block-1	$\begin{bmatrix} 1 \times 1, 64 \\ 3 \times 3, 64 \\ 1 \times 1, 256 \end{bmatrix} \times 3$	$56 \times 56 \times 256$
Residual Block-2	$\begin{bmatrix} 1 \times 1, 128 \\ 3 \times 3, 128 \\ 1 \times 1, 512 \end{bmatrix} \times 4$	$28 \times 28 \times 512$
Residual Block-3	$\begin{bmatrix} 1 \times 1, 256 \\ 3 \times 3, 256 \\ 1 \times 1, 1024 \end{bmatrix} \times 23$	$14 \times 14 \times 1024$
Residual Block-4	$\begin{bmatrix} 1 \times 1, 512 \\ 3 \times 3, 512 \\ 1 \times 1, 2048 \end{bmatrix} \times 3$	$7 \times 7 \times 2048$
Global average pooling	$1 \times 1 \times 2048$	
Feature classifier	20-d fc, SoftMax	

Residual Block Residual Block (RB) is the most vital element in the Feature Extractor. RB is based on the idea of skipping Blocks of convolutional layers by using shortcut connections. These shortcuts are useful for optimizing trainable parameters in back-propagation to avoid the vanishing/exploding gradients problem [38], which can help to improve the performance of extracting features.

As Fig. 6 shows, each RB consists of convolutional (Conv) layers and batch normalizations (BN) layers, Relu activation function and one shortcut connection. When a 256-d data flow is input into the RB, the number of channels will be compressed from 256 to 64 and expended from 64 to 256 in the last Conv layer so that the global features generated from the three Conv layers and the local features transmitted by the shortcut connection have the same number of channels, which is easy to add. The RB can be defined as Eq. 4.

$$Y = F(X, \{W_i\}) + X \tag{4}$$

Here X and Y are the input and output vectors of the layers considered. The function $F(X, \{W_i\})$ represents the residual mapping to be learned.

Classifier The Classifier is composed of fully connected layers, these fully connected layers perform a weighted sum of the input features and output the predicted class probabilities [40]. As Fig. 7 shows, features generated from Feature Extractor will be input to two hidden layers to calculate the weight. In the last layer of Classifier, the SoftMax function is employed to map features into possibilities of classes. Specially,

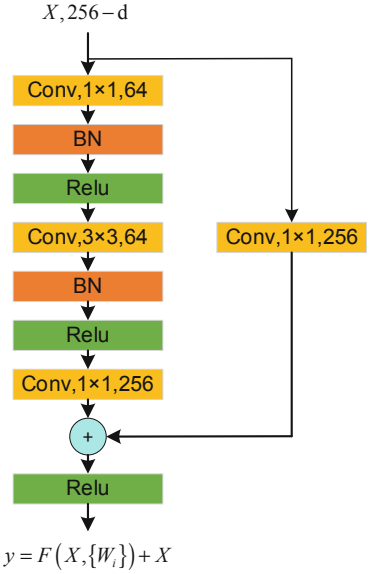

Fig. 6. The architecture of an RB example.

the SoftMax function converts the output values of multiple classes into probability distributions in the range [0, 1]. SoftMax function can be defined as Eq. 5.

$$\text{SoftMax}(z_i) = \frac{e^{z_i}}{\sum_{c=1}^{c} e^{z_c}} \tag{5}$$

where z_i is the output value of the i th node, and c is the number of output nodes, that is also the number of classifications.

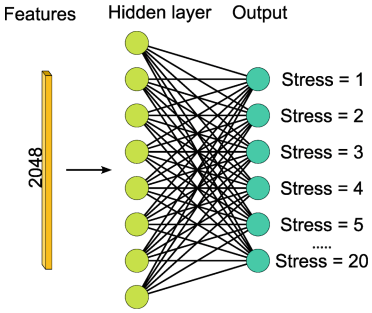

Fig. 7 The architecture of classifier.

Loss function In the iterations, the cross-entropy loss function is used to calculate the loss between true label and predicted label, and the loss value will be back-propagated to the network for updating the parameters, which leverages the model to correctly

extract local and global features from TF-images and get higher prediction accuracy. The cross-entropy loss function is defined as Eq. 6.

$$Loss = -\frac{1}{N}\sum_{i=1}^{N}\sum_{j=1}^{C} y_{i,j}\log(p_{i,j}) \tag{6}$$

where *Loss* represents the loss function, N is the sample numbers, C is the class numbers, $y_{i,j}$ presents the true label of sample i belongs to class j, $p_{i,j}$ presents the predicted label of sample i belongs to class j.

Optimizer The Adam optimizer is chosen in this study and defined as Eq. 7.

$$\begin{aligned} m_t &= \beta_1 m_{t-1} + (1-\beta_1) g_t \\ v_t &= \beta_2 v_{t-1} + (1-\beta_2) g_t^2 \\ \theta_{t+1} &= \theta_t - \frac{\eta}{\sqrt{v_t}+\varepsilon} m_t \end{aligned} \tag{7}$$

where, m_t represents first moment estimation, v_t represents second moment estimation, θ_t represents network parameters, g_t represents gradient, β_1 and β_2 represent exponential decay rate, ε represent represents a very small number, to prevent the case of dividing by zero.

3 Experiment

To validate the feasibility of USR-Net and address these limitations like random noise, continuous environment changes, measuring positions, and loading patterns, we design the two loading patterns experiments of reinforced concrete I-beam under non-controlled experimental environment conditions, collecting the coda wave signals of various stress values.

3.1 Experiment Design

Most coda wave measurement experiment objects are standard concrete square or cylindrical test Blocks, and the loading patterns are mostly uniaxial compression [1], but the concrete structure in the practical engineering of the section form is more diverse and the force form is more complex. Therefore, the previous experiment work is difficult to be applied in practical engineering. In order to improve the ap-plication feasibility of USR-Net in practical engineering, we choose the full-scale [41] model to observe the real response of concrete structure and the test is per-formed using real loads and boundary conditions. As the Fig. 8 shows, we design three-point bending and eccentric compression experiments with two loading pat-terns. The pulser on the one end transmits pulse wave through the I-beam under various stress and receivers on another end collect the coda waves. In this experiment, by changing the number of steel plate and the pressure value of hydraulic jack, we simulate the stationary stress changes. Besides, to test the universality, it costs plenty of time to conduct this experiment for collecting more data, which has been fully influenced by the environment changes.

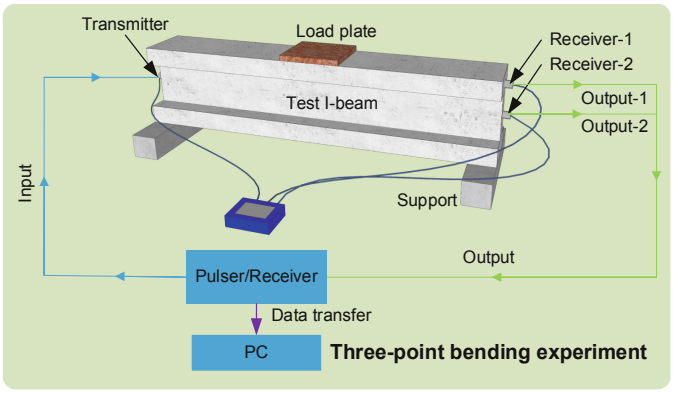

(a)

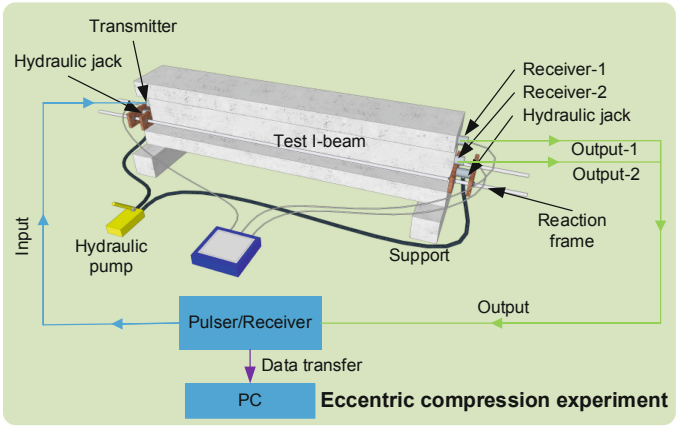

(b)

Fig. 8. Instrument layout. (a) Three-point bending ultrasonic experiment. (b) Eccentric compression ultrasonic experiment.

The response of concrete structure varies with different positions of section. In order to address the problems that traditional coda wave measurement only arrange the transducer in a specific position, we arrange the transducer of receiver-2 on the neutral axis of I-beam section and receiver-1 on the compressed and stretched part like Fig. 8. In the three-point bending experiment, the loading position is arranged the middle of I-beam to simulate the pure bending stress, and each load plate weighs 27.5 ± 0.4 kg. Similarly, we set the loading position in the down quarter of section. The loads are applied to the I-beam by the co-action of reaction frame and hydraulic jacks. Each load change is about 0.3 KN, which make sure loading smoothly changes.

3.2 Experiment Materials and Instruments

The full-scale I-beam model (the size as Fig. 9) is composed of C30-strength concrete with a mix ratio as presented in Table 2. The ultrasonic pulser and receiver device was a

nonmetallic transmittance instrument and transducer is the sandwich p-wave transducers (50 kHz).

Table 2. Mix ratio of C30 concrete.

Cement	Fine aggregate	Aggregate	Water	Fly ash	Mineral
1.00	2.50	3.85	0.55	0.22	0.16

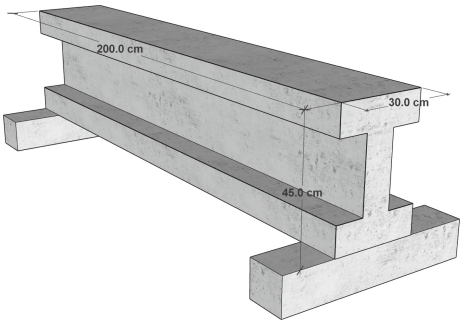

Fig. 9. Sizes of test I-beam.

Due to the signal quality related to the instrument parameters, it is essential to investigate and configure the instruments. Our team conducted an ultrasonic test of T-beam under three-point bending stress and optimized the parameters of the nonmetallic ultrasonic transmitter during the experiment before 2019. For this experiment, the parameters of non-metallic ultrasonic transmitter were selected through debugging, based on the experiences documented in the aforementioned literature. Table 3 summarizes the parameters associated with the nonmetallic ultrasonic transmitter, ensuring that the signal contains as much information as possible and transmittance receives a relatively stable signal.

Table 3. Instrument parameters.

Trigger delay [μs]	Sampling interval [μs]	Pulse width [μs]	Gain [dB]	Sampling length
9999	16	5	200	1024

4 Result and Discussion

To evaluate the effectiveness of USR-Net, 656000 signal samples, which consists of 20 classes from two I-beams of the three-point bending and eccentric compression experiment, are applied to predict stress labels. After STA and STF processing, TF-images

are generated for deep learning mode. To be specific, we use 524800 TF-images for training, 65600 TF-images for validation, and 65600 TF-images for testing. To establish the related labels with actual stress values, we perform the finite element analysis of three-point bending loading experiment and eccentric compression experiment under various loadings and acquire the maximal combined stress values (see Table 4). Then, the stress labels are encoded to one-hot format to facilize deep learning model training process. The experimental results demonstrate high prediction accuracy on our dataset. To further explore the performance of USR-Net, four indexes based on confusion matrix are calculated. Besides, we compare our model with popular non-DL algorithms, including Singular Value Decomposition (SVD), Support Vector Machine (SVM), Developed Support Vector Machine (DSVM), and Coda Wave Interferometry (CWI).

All samples were collected over a period of two years under changing environments, which can certainly verify the ability of resisting environmental interference.

Table 4. The stress of mid-span position via the finite element.

label	Max combined stress (*KPa*)	Shear stress (*KPa*)
0	118.5	63.5
1	144.1	71.6
2	169.7	79.7
3	195.3	87.8
4	220.9	95.9
5	246.5	104
6	272.1	112.1
7	297.7	120.2
8	323.3	128.3
9	348.9	136.4
10	374.5	144.5
11	400.1	152.6
12	425.7	160.7
13	451.3	168.8
14	476.9	176.9
15	502.5	185
16	528.1	193.1
17	553.7	201.2
18	579.3	209.3
19	604.9	217.4
20	630.5	225.5

4.1 Experimental Result

We train the deep learning model, Features Extractor and Classifier, with TF-images produce by applying STA and STF on signal samples. As Fig. 10 shows, with iteration increases, the accuracy of eccentric compression experiment (E-train) and three-point bending experiment (T-train) increases and achieves 99.99% accuracy on two loading mode. Even though there exist some fluctuation during training, for example, The loss for both E-train and T-train increases dramatically around the 20th iteration, the prediction accuracy converges to stable value.

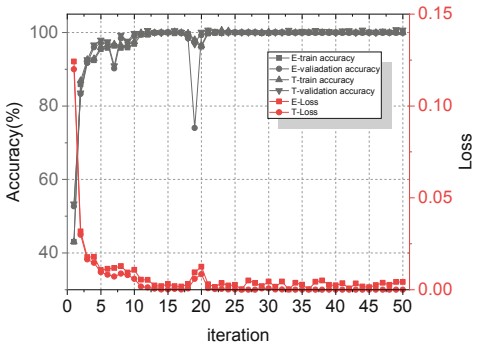

Fig. 10. The classification accuracy (left axis) and loss value (right axis) in the iteration of two experiments, where E represents the eccentric compression experiment and T represents the three-point bending experiment.

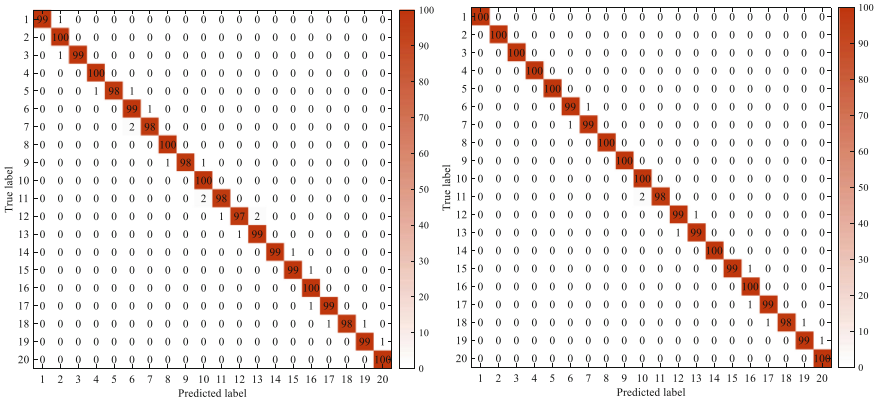

Fig. 11. The confusion matrix of three-point bending (left) and eccentric compression stress identification accuracy (right).

However, accuracy is not enough to reliably reflect the performance of the USR-Net. To Further evaluate the result, we build confusion matrix to calculate four indexes: accuracy, precision, recall and specificity. Accuracy represents the proportion of all correctly judged results of classification model in the total observed value. Precision

represents the proportion of the model prediction that is correct in all the results where the model prediction is positive. Recall represents the proportion of the model prediction that is correct in all the results where the true value is positive. Specificity represents the proportion of all results in which the true value is negative that the model's prediction is correct. Figure 11 demonstrates the confusion matrix of our model. According to the definition of four indexes as Eqs. 8–11, we can calculate accuracy, recall, precision, and specificity (see Fig. 12).

$$\text{Accuracy} = \frac{TP + TN}{TP + TN + FP + FN} \tag{8}$$

$$\text{Recall} = \frac{TP}{TP + FN} \tag{9}$$

$$\text{Precision} = \frac{TP}{TP + FP} \tag{10}$$

$$\text{Specificity} = \frac{TN}{TN + FP} \tag{11}$$

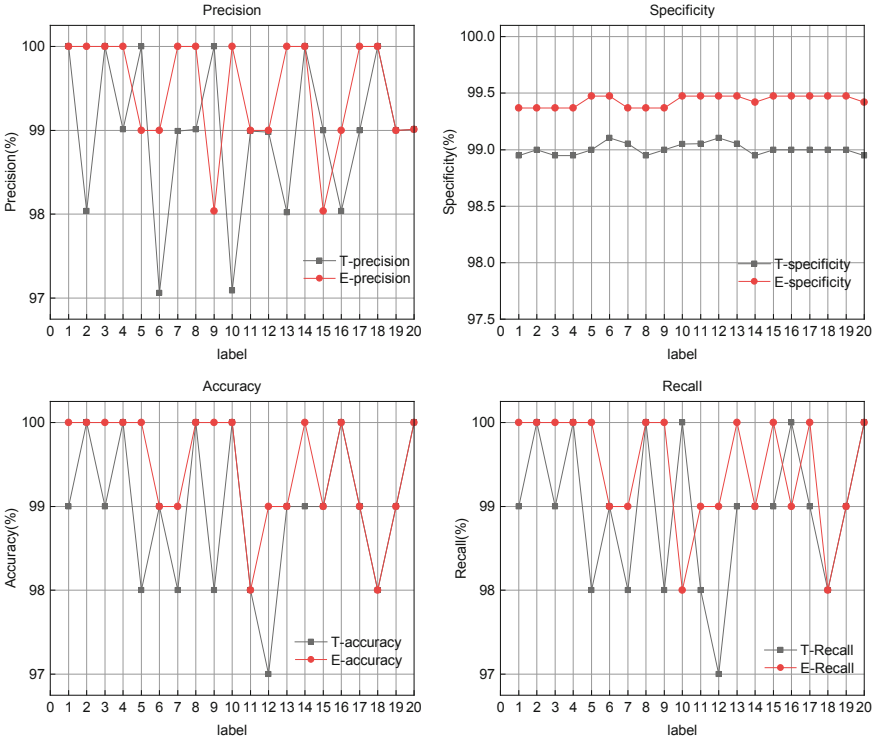

Fig. 12. The accuracy, recall, precision and specificity of USR-Net in three-point bending (T represents) and eccentric compression experiments (E represents).

4.2 Discussion

Comparison We compared the performance of USR-Net with the non-DL algorithms, but the non-DL algorithms evaluation index varies with the characteristic of them, such as the SVD utilizes correlation coefficient [42] to evaluate and CWI uses goodness of fit [43]. Specially, the correlation coefficient is a statistical measurement used to assess the strength of the linear relationship between two variables, and goodness of fit is a statistical measurement used in statistics to assess the fit degree of a statistical model. For the purpose of comparison, these evaluation indexes are all defined with the same physical meaning as classification accuracy and uniformly referred to as classification accuracy in the subsequent description. In the comparison, we use all samples to analyze, and calculate the average accuracy which is shown in Fig. 13. Comparing with traditional non-DL algorithms, the USR-Net proposed in this study has a higher average identification accuracy for its better feature extraction capability. For instance, USR-Net improve 17.5% and 15.9% of eccentric compression and three-point bending experiment than the popular non-DL algorithm CWI, which only gets 85% and 86.2% on our dataset.

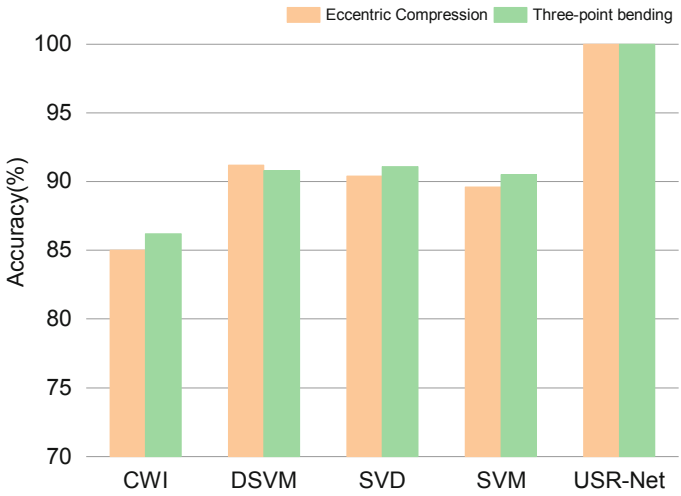

Fig. 13. Comparison with non-DL algorithms.

The verification of Kaiser effect As Fig. 10 shows, with the increase of number of iterations, the accuracy rises gradually, but when the numbers of iteration are 8 and 18, both the train accuracy and the validation accuracy suddenly decreased, we argued that is because the Kaiser effect [44] which refers to the phenomenon in which materials exhibit a characteristic pattern of stress-strain behavior during cyclic loading. Due to the existence of Kaiser effect, the concrete structure has a stress-memory effect, when a cycle of loading is complete and immediately unloading, the stress of concrete will not change and keep the state for a long time. Thus, another cycle of loading even begins, and the collected coda wave signals still present the state of last loading.

To verify the idea of Kaiser effect, we use the signals of loading level is 20 (the red label in Fig. 14) in the last loading cycle and the signals of loading level is 1 (the green

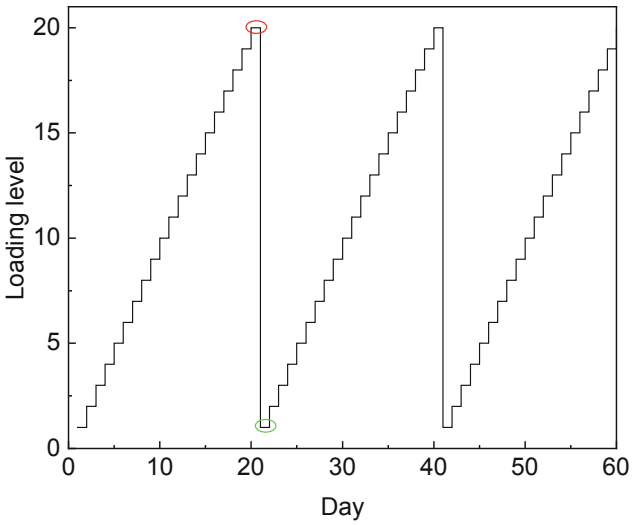

Fig. 14. Loading sequence.

label in Fig. 14) in the next loading level cycle to identify via USR-Net and non-DL algorithms. The result is shown in Table 5, we can see the results of SVD and CWI are not like the others, because the SVD and CWI mainly establish the mathematical linear model between the specific features and stress. Due to the interference from various factors, they cannot give the accuracy prediction like these labeled values. When identifying the label of 20, USR-Net, SVM, and DSVM can output the value corresponding to the label, moreover, SVD and CWI also give the relatively similar results that is relatively close to the actual stress. However, when identifying the label of 1 in the next cycle, the predict result of non-DL algorithms is similar to the label of 20 in the last cycle. Therefore, the Kaiser effect has significant influence in the coda wave signals in the coda wave measurement.

Table 5 The verify result of Kaiser effect via USR-Net and non-DL algorithms.

True label	Predicted label (convert to stress value, KPa)				
	USR-Net	SVD	CWI	SVM	DSVM
20 (630.5)	630.5	626.3	600.4	630.5	630.5
1 (144.1)	144.1	598.5	588.2	604.9	604.9

The performance of anti-noise We test the performance of anti-noise via adding random Gaussian white noise to raw signal and compare the identification accuracy of USR-Net and non-DL algorithms under different SNR. In the process of test, the TF-images generated from signals polluted by noise are input into USR-Net, and these signals are analyzed by non-DL algorithms, the accuracy of all methods is shown in Fig. 15.

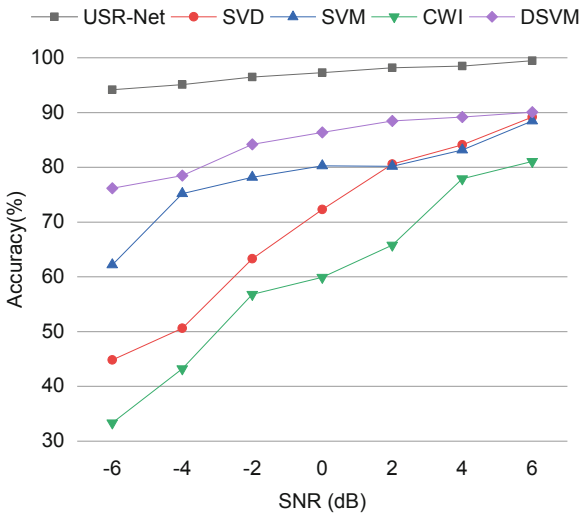

Fig. 15. The accuracy varies with SNR.

From Fig. 14, the USR-Net had the highest accuracy than other methods. Under SNR $= -6$dB, the accuracy of the USR-Net is still 94.2%, and the accuracy of SVD, SVM, CWI and DSVM are 44.8%, 62.2%, 33.3% and 76.2. The filter of USR-Net removes some noise in the signal processing, and after learning step by step, the deep learning model can correctly extract valuable features from noised TF-images. Besides, USR-Net has a multi-scale respective field and multi-channel feature fusion, which can capture richer features of TF-images. Therefore, USR-Net has the best classification effect in low-SNR environments and keep the good performance on anti-noise testing. Even when the SNR is more than 2dB, USR-Net shows a distinctive identification accuracy rate of 98.5% comparing with other coda wave measurement methods.

5 Conclusion

In response to the limitations in measuring reinforced concrete stress via ultrasonic coda wave, this study proposes the USR-Net, a method for combining the S-transform and deep learning model. USR-Net employs S-transform-based Time-frequency Filter to eliminate random noise and S-transform-based Time-frequency Analyzer to extract two-dimensional feature of the coda wave signal for generating TF-image. Then, Feature Extractor with Residual Blocks is applied to extract detailed valuable features from

the TF-images, which utilizes shortcut connection to maintain local features while feature map size reduces. Finally, Classifier takes use of linear layers to establish local and global features with actual stress labels. To evaluate the performance of USR-Net, we designed three-point bending and eccentric compression experiments and achieves the identification accuracy of 99.99% in two load patterns under continuous changing environment. Further, we explore the result of confusion matrix and use four indexes, accuracy, recall, precision, and specificity, to verify our model. Additionally, we compare USR-Net with some popular non-DL algorithms, which demonstrates USR-Net can achieves better results than other methods even under different noise condition. We also discuss about the Kaiser effect in coda wave stress measurement to explain the exceptional loss fluctuation. The good anti-noise performance and better identification accuracy of USR-Net enable it has application prospects in practical engineering. The USR-Net highlights the potential of deep learning algorithms in monitoring the health of reinforced concrete structures and contributes to the development of more precise and effective stress measurement techniques.

References

1. Jiang H, Zhang J, Jiang R, F.: Stress evaluation for rocks and structural concrete members through ultrasonic wave analysis. Journal of Materials in Civil Engineering 29(10), 04017172 (2017).
2. Castaneda, D. I, F.: New field-testing procedure for measuring residual stress in plain concrete pavements and structures. M.Sc. thesis, Univ. of Illinois at Urbana-Champaign, Champaign, IL (2010).
3. Herraiz, M., Espinosa, F.: Coda waves: A review. PAGEOPH 125, 499–577 (1987).
4. T. Planès, E. Larose, F.: A review of ultrasonic Coda Wave Interferometry in concrete. Cement and Concrete Research 53, 248–255 (2013).
5. Liu, Y., Guo, S., Xu, Y., & Xia, F.: Real-time monitoring of stresschanges in concrete using coda wave interferometry. Sensors 18(2), 626 (2018).
6. Snieder, R., Greötz, A., Douma, H., & Scales, F.: Coda wave interferometry for estimating nonlinear behavior in seismic velocity. Science 295(5559), 2253-2255 (2003).
7. Payan, F.: Coda wave interference for extracting the third-order nonlinear coefficient of concrete materials: functional relationship between the relative change rate of wave velocity and stress. Journal of Nondestructive Evaluation 28(1), 1-10 (2009).
8. Payan, C., Garnier, V., & Moysan, F.: Determination of third order elastic constants in a complex solid applying coda wave interferometry. Applied Physics Letters 94(1), 011904 (2009).
9. Hafiz, A., Schumacher, F.: Monitoring of Stresses in Concrete Using Ultrasonic Coda Wave Comparison Technique. J Nondestruct Eval 37, 73 (2018).
10. Clauß, F.; Epple, N.; Ahrens, M.A.; Niederleithinger, E.; Mark, F.: Correlation of Load-Bearing Behavior of Reinforced Concrete Members and Velocity Changes of Coda Waves. Materials 2022(15), 738 (2022).
11. Wang, X., Chakraborty, J. & Niederleithinger, F.: Noise Reduction for Improvement of Ultrasonic Monitoring Using Coda Wave Interferometry on a Real Bridge. J Nondestruct Eval 40, 14 (2021).
12. Grêt A, Snieder R, Scales J, F.: Time-lapse monitoring of rock properties with coda wave interferometry. Journal of Geophysical Research: Solid Earth (B3), 111 (2006).

13. Serra M, Festa G, Vassallo M, F.: Damage detection in elastic properties of masonry bridges using coda wave interferometry. Structural Control and Health Monitoring 24(10), e1976 (2017).
14. Onur Avci, Osama Abdeljaber, Serkan Kiranyaz, Mohammed Hussein, Moncef Gabbouj, Daniel J. Inman, F.: A review of vibration-based damage detection in civil structures: From traditional methods to Machine Learning and Deep Learning applications. Mechanical Systems and Signal Processing 147, 107077 (2021).
15. Zhang J, Han B, Xie H B, F.: Correlation between coda wave and stresses in uni-axial compression concrete. Applied Sciences 8(9), 1609 (2018).
16. M. Schimmel and J. Gallart, F.: The inverse S-transform in filters with time-frequency localization. IEEE Transactions on Signal Processing 53(11), 4417–4422 (2005).
17. N. Liu, J. Gao, B. Zhang, F. Li and Q. Wang, F.: Time–Frequency Analysis of Seismic Data Using a Three Parameters S Transform. IEEE Geoscience and Remote Sensing Letters 15(1), 142–146 (2018).
18. Das M K, Ari S, F.: Analysis of ECG signal denoising method based on S-transform. Irbm 34(6), 362–370 (2013).
19. Parolai S, F.: Denoising of seismograms using the S transform. Bulletin of the Seismological Society of America 99(1), 226–234 (2009).
20. S. S. Sahu, G. Panda and N. V. George, F.: An Improved S-Transform for Time-Frequency Analysis. 2009 IEEE International Advance Computing Conference, Patiala, India, 315–319 (2009).
21. N. Liu, J. Gao, B. Zhang, Q. Wang and X. Jiang, F.: Self-Adaptive Generalized S-Transform and Its Application in Seismic Time–Frequency Analysis. IEEE Transactions on Geoscience and Remote Sensing 57(10), 7849–7859 (2019).
22. E. Goceri, F.: Analysis of Deep Networks with Residual Blocks and Different Activation Functions: Classification of Skin Diseases. 2019 Ninth International Conference on Image Processing Theory, Tools and Applications (IPTA), Istanbul, Turkey, 1–6 (2019).
23. Sarwinda D, Paradisa R H, Bustamam A, F.: Deep learning in image classification using residual network (ResNet) variants for detection of colorectal cancer. Procedia Computer Science 179, 423–431 (2021).
24. Stockwell, R.G., Mansinha, L., Lowe, R.P., F.: Localization of the complex spectrum: the s transform. IEEE Trans. Signal Process 44(4), 998–1001 (1996).
25. Beuter C, Oleskovicz M. F.: S-transform: from main concepts to some power quality applications. IET Signal Processing 14(3), 115-123 (2020).
26. Stockwell, R.G, F.: A basis for efficient representation of the s-transform, Digit. Signal Process. 17(1), 371–393 (2007).
27. 28. Battisti, U., Riba, F.: Window-dependent bases for efficient representations of the stockwell transform. Appl. Comput. Harmon. Anal. 40(2), 292–320 (2016).
28. Wang, Y. F.: Efficient Stockwell transform with applications to image processing. PhD thesis, UWSpace, University of Waterloo (2011).
29. 30. Beuter, C. and Oleskovicz, F.: S-transform: from main concepts to some power quality applications. IET Signal Process. 14, 115-123 (2020).
30. Reddy, M.J.B., Raghupathy, R.K., Venkatesh, K.P., F.: Power quality analysis using discrete orthogonal s-transform (dost). Digit. Signal Process. 23(2), 616–626 (2013).
31. Wang, Y. Efficient Stockwell transform with applications to image processing. PhD thesis, UWSpace, University of Waterloo (2011).
32. B. Li and Y. He., F.: An Improved ResNet Based on the Adjustable Shortcut Connections. IEEE Access 6, 18967–18974 (2018).
33. Zhang T, Waqas M, Liu Z, F.: A fusing framework of shortcut convolutional neural networks. Information Sciences 579, 685–699 (2021).

34. 37. Wu, S., Zhong, S. & Liu, F.: Deep residual learning for image steganalysis. Multimed Tools Appl 77, 10437–10453 (2018).
35. Cai P, Sur S, F.: MilliPCD: Beyond Traditional Vision Indoor Point Cloud Generation via Handheld Millimeter-Wave Devices. Proceedings of the ACM on Interactive, Mobile, Wearable and Ubiquitous Technologies 6(4): 1–24 (2023).
36. He K, Zhang X, Ren S, F.: Deep residual learning for image recognition. Proceedings of the IEEE conference on computer vision and pattern recognition, 770–778 (2016).
37. Wen, L., Li, X. & Gao, L, F.: A transfer convolutional neural network for fault diagnosis based on ResNet-50. Neural Comput & Applic 32, 6111–6124 (2020).
38. Shafiq, M.; Gu, Z, F.: Deep Residual Learning for Image Recognition: A Survey. Appl. Sci. 12, 8972 (2022).
39. A. Jafar and L. Myungho, F.: Hyperparameter Optimization for Deep Residual Learning in Image Classification. 2020 IEEE International Conference on Autonomic Computing and Self-Organizing Systems Companion (ACSOS-C), Washington, DC, USA, 2020, 24–29 (2020).
40. Basha S H S, Dubey S R, Pulabaigari V, F.: Impact of fully connected layers on performance of convolutional neural networks for image classification. Neurocomputing 378: 112–119 (2020).
41. Bian X, Jiang H, Cheng C, F.: Full-scale model testing on a ballastless high-speed railway under simulated train moving loads. Soil Dynamics and Earthquake Engineering 66: 368–384 (2014).
42. Uchida, Y., Kanade, T., Shiozawa, D. F.: Thermoelastic Stress Measurement Using SVD Thermo-Component Analysis. Exp Mech 63, 337–347 (2023).
43. Stähler S C, Sens-Schönfelder C, Niederleithinger E., F.: Monitoring stress changes in a concrete bridge with coda wave interferometry. The Journal of the Acoustical Society of America 129(4), 1945–1952 (2011).
44. Shokouhi, P., Zoega, A., Wiggenhauser, F.: Nondestructive investigation of stress-induced damage in concrete. Adv. Civil Eng, 1–9 (2010).
45. Donoho D. De-noising by soft-thresholding. IEEE Trans Inform Theory, 41:613–27 (1995).